Oscillations of a flexible filament under surface gravity waves

Kamlesh Kumar, Vivek Kumar, and P. Deepu*
Department of Mechanical Engineering, Indian Institute of Technology Patna, Bihta, 801103, Bihar, India

Pritesh Ramya
Department of Mechanical Engineering, Indian Institute of Technology Palakkad, 678557, Kerala, India

(Received 3 February 2020; accepted 26 October 2021; published 10 November 2021)

This paper reports an experimental and theoretical investigation of the hydrodynamic interaction of a deformable structure with gravity waves. High-speed imaging and particle image velocimetry measurements were employed to analyze the oscillation characteristics of a cylindrical filament placed transversely in the flow generated due to gravity waves in a water channel. Based on the Euler-Bernoulli equation, we derive and solve a theoretical model to predict the oscillation dynamics of the elastic structure in two limiting cases: the inertia-dominated regime and drag-dominated regime. In the inertia-dominated regime the system exhibits resonance, while the frequency response of oscillations in the drag-dominated regime shows no resonance. Our results from experiments carried out on aquatic plants and silicone rubber fibers further corroborate the findings from the model in the inertialess regime. The quality factor of the oscillation response is used to explain the absence of resonance in the drag-dominated regime. We also address the question as to when the inertial effects can be neglected from the analysis.

DOI: 10.1103/PhysRevFluids.6.114004

I. INTRODUCTION

Flexible structures embedded in a relatively moving fluid are encountered in many applications, e.g., the paper industry [1], energy harvesting [2], and processing of composite materials [3]. In nature, the basilar membrane in the inner ear [4], cilia in the mammalian trachea [5], and biolocomotion [6] are a few examples. Understanding the complex multiscale nonlinear coupling between compliant biological structures and fluid motion is key to describing the underlying biophysical phenomena. For instance, vegetation plays a major role in the generation of wind turbulence [7], and in turn, wind affects the plant growth via inducing external mechanical forces on the plant [8] and the dynamics of seed dispersal [9].

Coupled dynamics of elastic-fluid systems has been the topic of many studies. Zhang *et al.* [10] observed that the response of an elastic filament embedded in a flowing soap film becomes unstable as the filament length is increased. Shelley *et al.* [11] studied the flapping behavior of a flaglike body in a water tunnel flow. Eloy *et al.* [12] investigated the flow-induced instability of a flexible plate in a wind tunnel. The results of Jung *et al.* [13] show that the wake structure behind an oscillating elastic loop in a fast-flowing soap film is akin to that of an oscillating bluff body. The flapping instability observed in these studies is a manifestation of the complex interplay among pressure forces, structural inertia, and rigidity.

A particular example of biological structures interacting with wavy fluid motion is aquatic plants, e.g., macrophytes (submergent, emergent, or floating water plants). They are vital to the

*Corresponding author: deepu@iitp.ac.in

aquatic ecosystem, because they act as a habitat and food and oxygen source for fishes and aquatic insects. The relative motion of the water exerts fluid stresses on the plants, especially for sessile plants, causing hydrodynamic forces to act on the plant. The plant, in turn, makes morphological adaptations to decrease the drag force to avoid its uprooting [14]. Motivated by such applications, a number of recent studies have investigated the oscillations of elastic structures, induced by unsteady fluid flow. The flexible structures studied include blades [15,16], rectangular filaments [17], or flexible aquatic plants [18]. In experiments, the unsteady flow could be realized by support vibration of the structure [16], using wave generators [15,17] or in natural aquatic systems [18].

Luhar and Nepf [15] proposed that plant movement in a wave-induced unsteady flow is governed by the following two dimensionless parameters: (1) Cauchy number, Ca (ratio of the hydrodynamic forcing to the restoring elastic force), and (2) the ratio of blade length to the wave orbital excursion, $\tilde{L}$. They showed that for Ca $<$ 1 (stiff stem), the plant exhibits oscillatory movement. On the other hand, for Ca $>$ 1 (flexible stem), plants tend to bend, leading to reduction in flow resistance. For $\tilde{L} > 1$ (small wave excursions), plants exhibit a swaying motion, while the opposite regime of $\tilde{L} < 1$ (large excursions) leads to canopy flattening. Leclercq and de Langre [16] investigated the reconfiguration and the resulting internal stress of two-dimensional polymer blades in a flow field that is sinusoidally varying in time but spatially uniform. They delineated four different kinematic regimes of the structure response, depending on the amplitude and frequency of the oscillating flow relative to the dimensions and the natural frequencies of the blade, respectively. The internal stresses were observed to reduce in the drag-dominated region (when the drag dominates the fluid inertia). They also discussed the resonant excitation of the blade in fluid inertia-dominated regime, in the absence of the structural inertia. Mullarney and Henderson [18] developed a theoretical model based on Euler-Bernoulli formulation of a cantilever beam to analyze the motion of single stem vegetation and tested the model with motion of the sedge *Schoenoplectus amaricanaus* in natural salt marshes. They estimated that wave height attenuation due to flexible vegetation is nearly 30% of that due to rigid stem vegetation.

However, many of these works focus on investigating the hydrodynamic forces induced on the structure and the effect of fluid-structure coupling on the flow field itself. The goal of the present study is to investigate the interaction of surface gravity waves with cylindrical filaments and single-stem aquatic plants and address the possibility of resonant excitation. The major contribution of the present work is a theoretical model that describes the dynamics of a deformable cylindrical fiber fixed transversely in a flow field which exhibits single-tone periodicity in both space and time. We predict the response of the fiber in two limits: the inertialess (drag-dominated) oscillations and the inertia-dominated oscillations. Note that the resonance discussed here is due to structural inertia and not due to fluid inertia as in Ref. [16]. Also, Mullarney and Henderson [18] consider a random velocity field existing in a natural salt marsh and do not discuss resonance. In the inertialess regime, the amplitude of the fiber remains bounded (even in the absence of structural damping), precluding the existence of resonant oscillations. In the inertialess regime, the theoretical results are validated numerically and by experiments carried out on aquatic plants and synthetic fibers submerged in a surface gravity wave flow field generated in a water channel. High-speed imaging and particle image velocimetry (PIV) techniques were used to analyze the filament dynamics and fluid velocity field. Waves at different frequencies, wave numbers, and amplitudes were generated.

II. EXPERIMENTAL SETUP

A water channel (1500 mm long, 240 mm wide, and 240 mm high) made of glass sheets was equipped with a rectangular wave-generator plate at one end. The frequency and amplitude of the stroke of the plate was controlled using a servo-actuator [see Fig. 1(a)]. The rotary motion of two Nema 17 motors, each having a holding torque of 4.2 kgcm, was converted to reciprocating motion of the wave generating using a rack and pinion arrangement. A damper, made of stone pellets, was installed at the other end of the tank to minimize the wave reflections, ensuring the generation of traveling surface waves. The flexible filament of length $L = 12$ cm and diameter

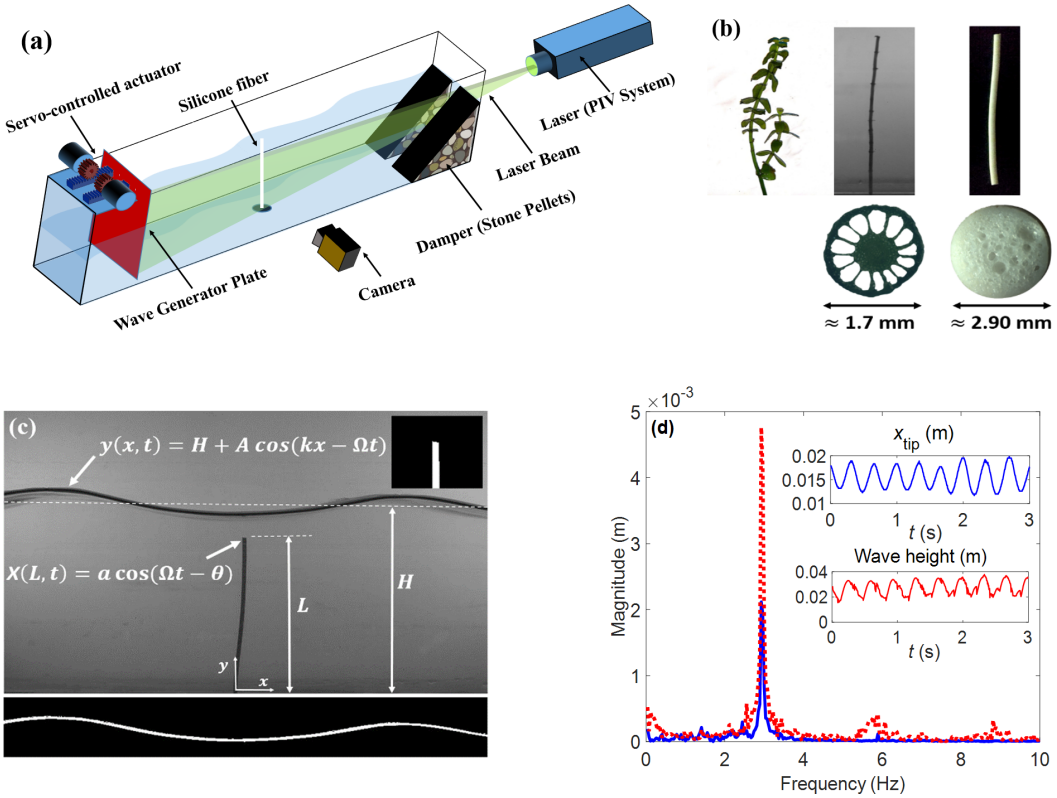

FIG. 1. (a) Schematic of the experimental setup showing the water channel with the wave generator. (b) Photographs of the aquatic plant (left), aquatic plant without leaf (center), and silicone rubber fiber (right). The microscopic images of their respective cross sections are provided at the bottom. (c) Experimental image of silicone rubber fiber submerged under the water wave. The equations of the wave profile and the displacement of the fiber tip and the various parameters of the problem are shown. Inset and the bottom image show the binary images of the fiber tip and water wave, respectively, obtained after thresholding the original images. (d) FFT spectrum of the displacement of the tip of the fiber (blue solid curve) and the height of the water wave (red dashed curve). Insets show the corresponding time-series data. Since the amplitude and frequency of the oscillations are of interest, the data are measured from arbitrary reference points in the image. $\Omega = 18.38$ rad/s, $k = 29.42$ m^{-1}, $A = 8.03$ mm.

$d = 2.90$ mm was fixed at the center of the tank vertically. Experiments were carried out on silicon rubber fibers (density, $\rho \approx 800$ kg/m^3; Young's modulus, $E \approx 2.9 \times 10^5 \pm 1.1 \times 10^5$ N/m^2) and one specimen of the aquatic plant, *Bacopa caroliniana* ($\rho \approx 750$ kg/m^3, $E = 7.51 \times 10^6$ Pa [19]). They are referred to as simply fiber and plant, respectively, hereafter. The Young's modulus for the fiber was measured by conducting tensile tests on the specimens. *Bacopa caroliniana* [see Fig. 1(b)] is an aquatic plant found in marshy areas in the southern region of the United States and the southern region of Korea.

A high-speed camera (Phantom v7.3) acquired the images of the water wave and the fiber motion at 250 frames per second. Image analysis was carried out using in-house MATLAB scripts to determine the displacement of the fiber and water wave features such as wave number ($k = 2\pi/\lambda$; λ is the wavelength), angular frequency ($\Omega = 2\pi f$, with f denoting the frequency), and amplitude (A). Each grayscale frame of the videos captured was converted to a binary image using a gray threshold [see Fig. 1(c)]. The MATLAB scripts extract the time-series data of the desired parameters from consecutive frames of the video. Images were captured at a spatial resolution in the range

TABLE I. Experimental and theoretical results for the silicone rubber fiber.

Exp. no.	Ω (rad/s)	k (1/m)	A (mm)	L (m)	H (m)	a_{Exp}(mm)	a_{Theory} (mm)
1	14.99	24.15	7.57	0.12	0.17	3.82	1.80
2	12.60	16.88	7.40	0.12	0.17	5.89	3.12
3	14.73	18.45	12.44	0.12	0.17	4.34	4.77
4	16.10	21.47	16.42	0.12	0.17	4.08	4.98
5	16.75	25.28	7.21	0.12	0.15	2.05	2.71
6	19.86	34.46	7.21	0.12	0.15	2.20	1.70
7	15.01	21.49	9.07	0.12	0.15	5.39	4.21
8	18.38	32.15	5.10	0.12	0.15	2.51	1.33
9	14.89	19.56	13.33	0.12	0.15	6.92	6.97
10	16.16	23.85	10.49	0.12	0.15	5.26	4.29
11	14.40	20.38	5.75	0.12	0.15	3.70	2.80
12	16.67	25.08	9.05	0.12	0.15	1.79	3.45
13	19.83	35.17	8.16	0.12	0.15	1.75	1.86
14	14.99	20.11	15.30	0.12	0.15	4.85	7.74
15	18.38	29.91	7.89	0.12	0.15	2.06	2.33
16	14.86	19.81	11.70	0.12	0.15	6.21	6.01
17	19.31	33.82	7.15	0.12	0.15	2.21	1.74
18	16.06	23.39	12.43	0.12	0.15	4.03	5.21
19	19.41	39.28	5.73	0.125	0.15	2.17	1.28
20	16.33	29.52	6.87	0.125	0.15	2.89	2.36
21	13.56	23.18	7.09	0.125	0.15	5.50	3.32

of 3.5×10^{-5} to 4.9×10^{-4} m/pixel for measuring the tip deflection. However, for wave surface elevation, the experiments had to be recorded at spatial resolution in the range of 2.9×10^{-4} to 4.9×10^{-4} m/pixel, in order to obtain a bigger field of view.

Instantaneous 2D velocity field of the fluid, $\boldsymbol{U}(x, y, t) \equiv u\hat{\boldsymbol{i}} + v\hat{\boldsymbol{j}}$, was measured using the PIV technique. Here $\hat{\boldsymbol{i}}$ represents the unit vector in the x direction (direction of traveling wave) and $\hat{\boldsymbol{j}}$ represents that in the y direction (measured from the bottom of the liquid layer). The fluid (water) was seeded with silver-coated neutrally buoyant tracer particles (diameter 14 μm), and the vertical longitudinal plane (field of view 228.8 mm × 228.8 mm) containing the fiber was illuminated using a double-pulsed Nd-YAG laser (pulse frequency 15 Hz). A charge-coupled device camera (resolution 2048 × 2048 pixels) recorded the particle images. Subsequently, the fluid velocity field was obtained using INSIGHT 4G (TSI Inc.) PIV software with interrogation windows of 104 pixels × 104 pixels. The average wavelength of the surface wave observed in the experiments is of the order of 10 cm, which is much larger than the capillary length scale. Hence, the waves observed in the present study are indeed gravity waves [20]. Experiments were carried out with different values of λ, Ω, A and the height of the water layer H. Experimental conditions and results are presented in Tables I and II.

The range of the parameters was selected so that linear, travelling, sinusoidal gravity waves could be realized in the experiments, as shown in Fig. 1(c). In order to ensure that the waves are linear, only waves with $A/H < 0.10$ are considered. However, very low wave amplitudes were avoided as they resulted in insignificant response of the fiber. Also note that since $\frac{A}{L} < 1$ in our experiments, according to the amplitude-frequency space of [16] the fiber response is expected to be in the static reconfiguration regime. The data acquisition was started after the transients have decayed. In the steady-state conditions, the filament was observed to oscillate in its first mode. Fast Fourier transform (FFT) spectra of the measured water wave height and the displacement of the free tip of the fiber show that both data have exactly the same dominant frequency [see Fig. 1(d)]. This implies

TABLE II. Experimental and theoretical results for the plant.

Exp. no.	Ω (rad/s)	k (1/m)	A (mm)	L (m)	H (m)	a_{Exp}(mm)	a_{Theory} (mm)
1	16.72	23.23	6.16	0.12	0.15	2.57	2.61
2	19.97	34.03	5.25	0.12	0.15	3.83	1.27
3	15.06	22.56	8.75	0.12	0.15	3.76	3.85
4	12.50	19.08	4.15	0.12	0.15	3.28	2.17
5	18.44	29.47	7.00	0.12	0.15	3.38	2.13
6	14.70	21.76	11.00	0.12	0.15	5.32	5.06
7	19.32	37.07	9.16	0.12	0.15	3.45	1.92
8	16.20	25.59	10.31	0.12	0.15	4.15	3.85

that the oscillatory velocity field induced by the traveling water wave exerts a periodic force on the filament, and thus the filament can be modeled as a forced harmonic continuous system.

III. THEORETICAL DISCUSSION

The fiber deflection in the transverse direction $X(y, t)$, where $y \epsilon [0, L]$, is modeled as a cantilever, using the Euler-Bernoulli beam equation. Balancing the inertial, Froude-Krylov [15], added-mass, elastic, buoyancy, and drag forces acting per unit length of the filament we get

$$(\rho_s + \rho_f)\tilde{A}\frac{\partial^2 X}{\partial t^2} - \rho_f C_m \tilde{A}\frac{\partial U_r}{\partial t} = -EI\frac{\partial^4 X}{\partial y^4} - (\rho_f - \rho_s)g\tilde{A}\frac{\partial X}{\partial y} + \frac{C_D \rho_f r}{2}u_{\text{tip}}\left(u - \frac{\partial X}{\partial t}\right). \quad (1)$$

Here ρ_s is the density of the filament material, ρ_f is the fluid density, $\tilde{A}$ is the cross-sectional area of the fiber, C_m is the added mass coefficient, U_r is the relative velocity of the fluid with respect to the fiber, E is Young's modulus of the fiber material, $I = \pi d^4/64$ is second moment of area of the fiber, C_D is the drag coefficient, r is the radius of the fiber, and d is the diameter of the fiber. Since the cross section of the plant is observed to be not fully solid [see Fig. 1(b)], the second moment of the area for the plant was calculated numerically from the microscopic images. The linearized drag term (last term) is similar to that used in Ref. [18], except that the characteristic velocity is taken as the maximum fluid velocity at the tip of the fiber, u_{tip}. The average Reynolds number (based on fiber diameter and u_{tip}) observed in the experiments is of the order of 100, and hence we put $C_D = 3$ [18,21]. Axial tension in the beam is neglected, as the major motion is in the transverse direction and buoyancy is found to be negligible (shown later).

u in Eq. (1) is taken to be that of the potential flow velocity field induced in a layer of fluid due to the surface gravity wave, described by $y = H + A\ \cos(kx - \Omega t)$, where y is from the bottom of the liquid layer and H is the depth of the liquid layer. This represents a wave traveling in the positive x direction, and in the limit of small A/H (i.e., linear wave), it can be shown that [20]

$$u = \frac{A\Omega \cosh(ky)\cos(kx - \Omega t)}{\sinh(kH)}. \quad (2)$$

Also note that $u_{\text{tip}} = \frac{A\Omega \cosh(kL)}{\sinh(kH)}$. The potential flow approximation is justified, because the viscous effect is dominant within a fluid layer of thickness δ_v near the bottom wall of the tank [20]. The thickness of the Stokes layer $\delta_v \sim \sqrt{\frac{\nu}{\Omega}}$, where $\nu \sim O(10^{-6}\ \text{m}^2/\text{s})$ is kinematic viscosity of the fluid, and $\Omega \sim O(10\ \text{s}^{-1})$ is the wave frequency. Thus $\delta_v \sim O(10^{-2}\ \text{m})$, which is small compared to H; thus, most of the fluid layer thickness may be assumed to be in the inviscid region. The comparison of PIV measurements with the potential flow results further confirm this [see Fig. 2(c)].

Another critical assumption involved is that the interaction between the fluid and fiber is modeled using a one-way-coupling approach. In other words, the fluid flow field affects the fiber, but not vice versa, due to the small size and deflection of the fiber. This is corroborated by the PIV measurements, showing that the velocity field around the fiber agrees reasonably well with the theoretical one [see Fig. 2(a) vs Fig. 2(b)]. Further, absence of any noticeable vortex shedding around the fiber shows that

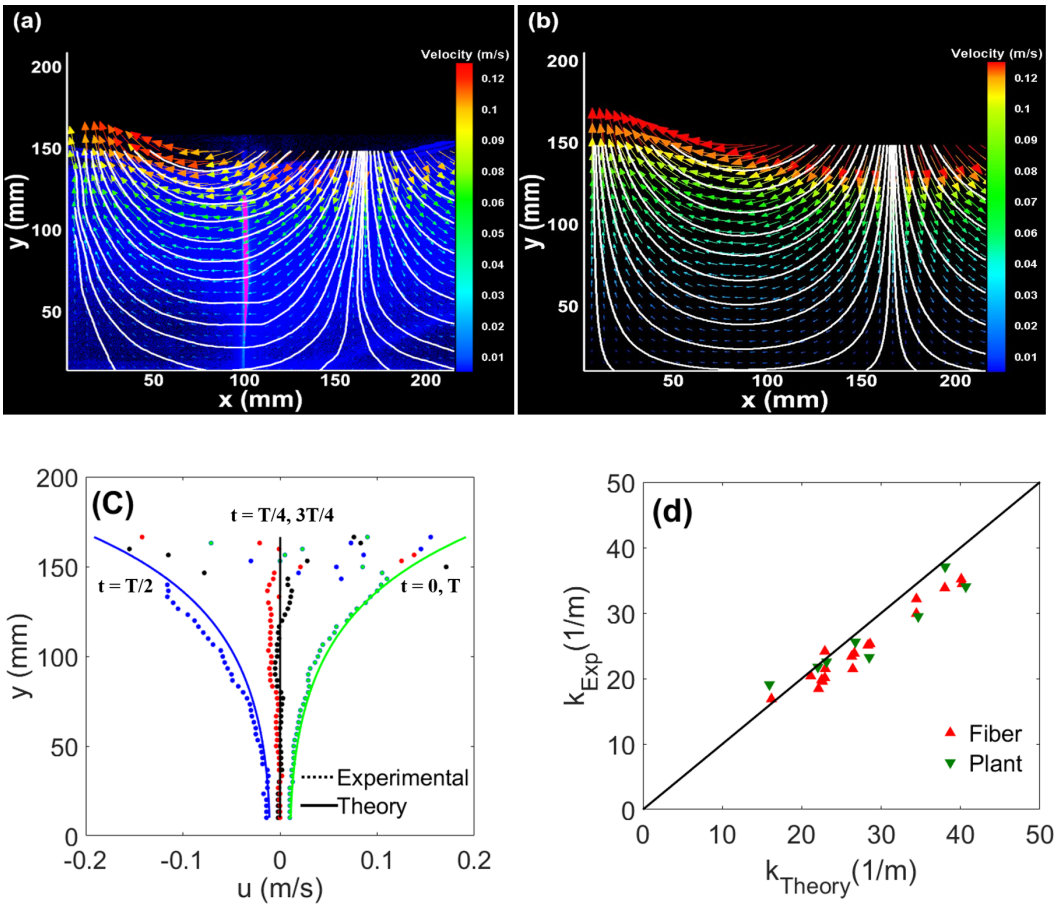

FIG. 2. (a) Instantaneous 2D velocity field and streamlines measured using PIV technique. $\Omega = 15.01$ rad/s, $k = 21.49$ m^{-1}, $A = 9.07$ mm. The camera was focused on the vertical plane containing the fiber. For clarity, the surface wave and the fiber (the vertical magenta line at $x \approx 100$ mm) at the same instant have been superimposed. (b) Corresponding velocity field and streamlines predicted by the theory. The color map shows the magnitude of velocity in units of m/s. (c) Comparison of experimental and theoretical flow velocity profiles at different times at a fixed x. $\Omega = 15.01$ rad/s, $k = 21.49$ m^{-1}, $A = 9.07$ mm (d) Comparison of theoretical wave number vs experimental wave number.

the presence of the fiber does not disturb the velocity flow field. The time-series data of measured and predicted velocities at a fixed point in the flow field [see Fig. 2(c)] further corroborate the fact that the experimentally realized velocity field agrees with the theoretical velocity field induced by the gravity wave. An additional check is possible by comparing the measured wave number with the theoretical wave number predicted by the dispersion relation for gravity waves given by

$$\Omega = \sqrt{gk \tanh(kH)}. \tag{3}$$

For all the experiments performed, $\tanh(kH) \approx 1$, i.e., the waves are deep-water waves. Therefore, the above formula can be further simplified to $\Omega^2 = gk$, which enables us to predict the theoretical values of k for the different set of experiments. The comparison is presented in Fig. 2(d).

We use L, $1/\Omega$, $L\Omega$ as the characteristic scales for length, time, and velocity to nondimensionalize the beam equation as

$$\bar{\rho}\frac{\partial^2 X^*}{\partial t^{*2}} - \tilde{\rho}\left(\frac{\partial u^*}{\partial t^*} - \frac{\partial^2 X^*}{\partial t^{*2}}\right) = -\frac{\partial^4 X^*}{\partial y^{*4}} - \bar{g}\frac{\partial X^*}{\partial y^*} + \bar{\mu}\left(u^* - \frac{\partial X^*}{\partial t^*}\right), \tag{4}$$

where $\bar{\rho} = (\rho_s + \rho_f)\frac{\tilde{A}L^4\Omega^2}{EI}$, $\tilde{\rho} = \rho_f C_m \frac{\tilde{A}L^4\Omega^2}{EI}$, $\bar{g} = (\rho_f - \rho_s)\frac{g\tilde{A}L^3}{EI}$, and $\bar{\mu} = \frac{C_D\rho_f r\Omega L^4 u_{\text{tip}}}{2EI}$, representing the nondimensional inertia with Froude-Krylov, added mass, buoyancy, and drag forces, respectively. The asterisk superscript on a variable indicates the corresponding dimensionless variable. Note that the nondimensional group, $\bar{\mu}$, has been identified in previous studies. Its definition is qualitatively similar to the Cauchy number described by Leclercq and de Langre [16], the inverse of dimensionless stiffness defined by Mullarney and Henderson [18], and Ca$\tilde{L}$ of Luhar and Nepf [15]; the exact expression is different due to the differences in the geometry of the structure and in the velocity scales employed in the present study.

IV. RESULTS AND DISCUSSION

A. Comparison of viscous theory and experiment

For the present experiments, $\rho_s \sim O(10^3\ \text{kg/m}^3)$, $\rho_f \sim O(10^3\ \text{kg/m}^3)$, $\tilde{A} \sim O(10^{-6}\ \text{m}^2)$, $\Omega \sim O(10\ \text{s}^{-1})$, $L \sim O(10^{-1}\ \text{m})$, $E \sim O(10^5\ \text{N/m}^2)$, $I \sim O(10^{-12}\ \text{m}^4)$, and $C_m \sim O(1)$ [15]. Thus, $\frac{\tilde{\rho}}{\bar{\mu}} \sim O(\frac{r}{A}) \sim O(0.1)$, indicating that in the present simplified model, we can neglect the inertia term (including Froude-Krylov force), the effect of which will be discussed later. Note that $\frac{\bar{\mu}}{\bar{\rho}}$ can be considered as the equivalent Keulegan-Carpenter number [22] in the problem. Further, $\frac{\tilde{\rho}}{\bar{\mu}} \sim O(0.1)$ and $\frac{\bar{g}}{\bar{\mu}} \sim O(0.001)$; hence we can neglect the added mass effect and buoyancy term from Eq. (4) to obtain

$$\bar{\mu}\frac{\partial X^*}{\partial \mathrm{t}^*} = -\frac{\partial^4 X^*}{\partial \mathrm{y}^{*4}} + \bar{\mu}u^* = -\frac{\partial^4 X^*}{\partial y^4} + \bar{\mu}\frac{A^*\cosh(k^*y^*)\cos(k^*X^* - t^*)}{\sinh(k^*H^*)}. \tag{5}$$

The boundary conditions are $X^*(0,t^*) = 0$, $\frac{\partial X^*}{\partial \mathrm{y}^*}(0,t^*) = 0$, $\frac{\partial^2 X^*}{\partial \mathrm{y}^{*2}}(1,t^*) = 0$, $\frac{\partial^3 X^*}{\partial \mathrm{y}^{*3}}(1,t^*) = 0$. The first two conditions describe the zero-deflection and zero-slope conditions at the fixed end of the beam, while the last two conditions describe the zero shear force and bending moment condition at the free end of the beam. The problem is solved by using the finite difference method with the zero deformation initial condition. An analytical solution is possible by assuming that the transverse deflection X^* is small, so that in the last term in Eq. (5) we can use the following approximation:

$$\cos(k^*X^* - t^*) \approx \cos(t^*). \tag{6}$$

The validity of this assumption will be examined later. Thus, we have

$$\bar{\mu}\frac{\partial X^*}{\partial t} + \frac{\partial^4 X^*}{\partial y^{*4}} = F(y^*)\cos(t^*), \tag{7}$$

where $F(y^*) = \bar{\mu}\frac{A^*\cosh(k^*y^*)}{\sinh(k^*H^*)}$.

The associated homogeneous boundary value problem admits a separable solution of the form $\sum_{j=1}^{\infty} Y_j(y^*)T_j(t)$, where $Y_j(y^*)$ represents the jth mode shape of the transverse vibration of the beam and can be derived as (see Ref. [23] or the appendix of Ref. [18])

$$Y_j(y^*) = [\sin\eta_j y^* - \sinh\eta_j y^* + D_j(\cos\eta_j y^* - \cosh\eta_j y^*)]. \tag{8}$$

Here $D_j = \frac{\cos\eta_j + \cosh\eta_j}{\sin\eta_j - \sinh\eta_j}$ and the eigenvalue η_j satisfies the characteristic equation $\cos(\eta_j)\cosh(\eta_j) = -1$. The first root of this equation is $\eta_1 = 1.875$.

Subsequently we seek the harmonic response solution to Eq. (7) of the form

$$X_V^*(y^*,t^*) = \mathrm{Re}\left[\sum_{j=1}^{\infty} C_j Y_j(y^*)e^{it^*}\right], \tag{9}$$

where i is the complex unit and Re[·] denotes the real part, and the subscript V denotes that it is a viscous-dominated solution. Substituting this ansatz into Eq. (7) and using orthogonality properties

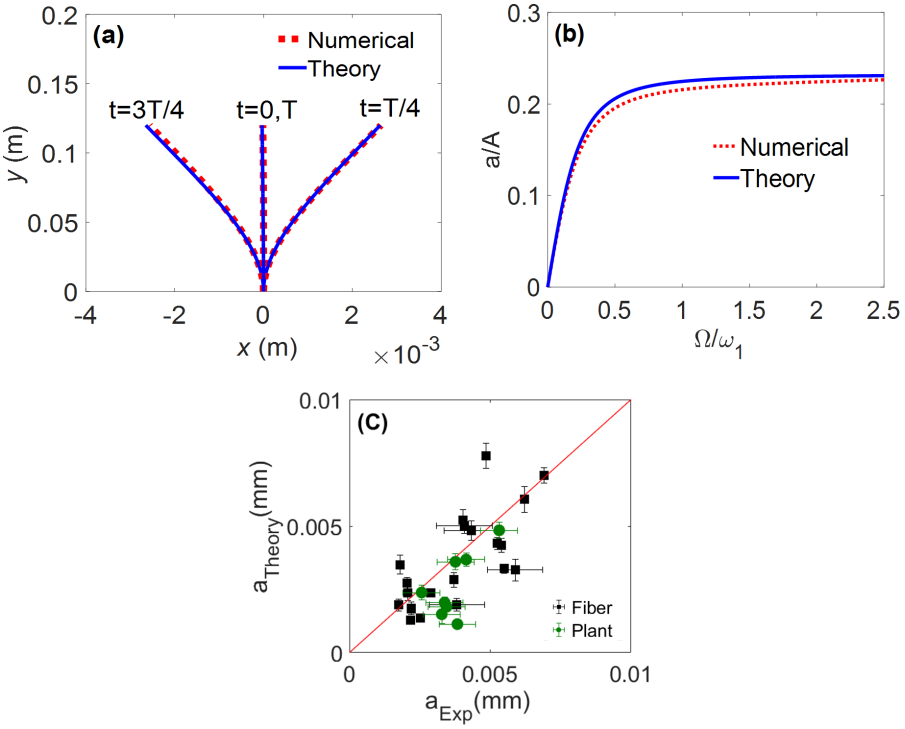

FIG. 3. (a) Instantaneous positions of the filament, as predicted by the theory [Eq. (11)] and numerical solution of Eq. (7), at different time instants in a steady-state oscillation cycle. T denotes the time period of oscillation. $\Omega = 16.66$ rad/s, $k = 24.66$ m^{-1}, $A = 9.2$ mm. (b) Response curve (numerical and theoretical) for drag-dominated oscillation at $k = 35$ m^{-1}, $A = 10$ mm. (c) Parity plot between the experimentally observed filament tip amplitude and the corresponding theoretical prediction. See Tables I and II for the data. The error bars on the experimental values represent two times the spatial resolution employed, while those on the theoretical results indicate the variation due to uncertainties in the measured wave amplitude and wave number.

of the eigenfunctions [23], we get

$$C_j = \frac{1}{(i\bar{\mu} + {\eta_j}^4)} \times \frac{\int_0^1 [F(\xi) Y_j(\xi)] d\xi}{\int_0^1 Y_j(\xi)^2 d\xi} \tag{10}$$

with ξ denoting the dummy variable of integration. Since only the first mode of vibration ($j = 1$) is observed in the experiments, we finally have the solution given by

$$X_V^*(y^*, t^*) = \frac{\int_0^1 F(\xi) Y_1(\xi) d\xi}{\int_0^1 Y_1(\xi)^2 d\xi} \times \frac{Y_1(y^*)}{\sqrt{({\eta_1}^8 + \bar{\mu}^2)}} \cos(t^* - \theta), \tag{11}$$

where $\theta = \tan^{-1}(\frac{\bar{\mu}}{{\eta_1}^4})$.

Figure 3(a) presents the instantaneous positions of the filament predicted by the theory [Eq. (11)] for a typical case. The numerical solution of Eq. (7) is also presented for comparison, showing that the theory is able to capture the evolution of the filament oscillations fairly accurately. Subsequently, Fig. 3(b) presents a typical response curve of the filament, where we have used the ratio of the amplitude of oscillation of the free end of the filament to the wave amplitude, i.e., $\frac{a}{A}$, as a measure of response. The excitation frequency, Ω on the abscissa is normalized using the first natural frequency of the cantilever, which will be derived later. Though natural frequency of the beam is irrelevant

in the inertialess limit, we use it for normalization to demonstrate the absence of resonance. The numerical and theoretical results agree fairly well with each other, except at large amplitudes of response. This is expected, as the assumption leading to Eq. (6) is valid only at small deflections. Note that the amplitude plateaus at large driving frequencies, which is expected due to the diffusion-like (as opposed to wavelike) nature of Eq. (7).

Since the experiments are carried out at small amplitudes, either theoretical or numerical results can be compared with the experiments to verify the model. Figure 3(c) shows the parity plot between the experimentally measured oscillation amplitude of the free end of the filament and the theoretical prediction [Eq. (11)]. Experimental results on fiber as well as plants are included in the plot. It can be concluded that the model provides a reasonably accurate prediction of the oscillation dynamics of the filament. It is worth mentioning that the model involves no fit parameters. Yet the majority of the data points lie within a tolerance of $\pm 20\%$. A potential source of error, besides the neglect of inertia term, is the uncertainty in C_D, which is assumed to be a constant (corresponding to a smooth nonoscillating cylinder in cross-flow). However, in the literature there exists a number of correlations for C_D in terms of the Reynolds number, specifically for moving vegetation [24,25]. The other sources of error include experimental error in the determination of Young's moduli, possible inhomogeneity in the modulus of the aquatic plant, and usage of the linearized Euler-Bernoulli equation. Note that due to the uncertainty in determining the moment of inertia of the original specimen, we perform experiments on the plant after removing the leaves, as shown in Fig. 1(b).

B. Response of the fiber in other regimes

We turn now to discuss the inviscid forced oscillations of the fiber, i.e., Eq. (4) in the limit of $\bar{\mu} \to 0$. The resulting equation can be solved (by the same procedure as explained above) to get

$$X_{\mathrm{I}}^*(y^*, t^*) = \frac{\int_0^1 P(\xi) Y_1(\xi) d\xi}{\int_0^1 Y_1(\xi)^2 d\xi} \times \frac{Y_1(y^*)}{({\eta_1}^4 - \hat{\rho})} \sin(\pi + t^*), \tag{12}$$

where $P(\xi) = \tilde{\rho} \frac{A^* \cosh(k^* \xi)}{\sinh(k^* H^*)}$ and $\hat{\rho} = \bar{\rho} + \tilde{\rho}$, which represents the combined effect of inertia and added mass. Clearly the solution exhibits resonance when ${\eta_1}^4 - \hat{\rho} = 0$, or equivalently $\Omega = \omega_1$, the fundamental natural frequency of the system given by

$$\omega_1 = {\eta_1}^2 \sqrt{\frac{EI}{(\rho_{\mathrm{s}} + (1 + C_m)\rho_{\mathrm{f}}) \tilde{A} L^4}}. \tag{(13)}$$

For the 0.12-m-long fiber considered in the present study, $f_1 = \frac{\omega_1}{2\pi} = 0.3$ Hz.

We also present the solution of Eq. (4) by neglecting only the buoyancy term. Thus Eq. (4) can be rewritten as

$$\hat{\rho} \frac{\partial^2 X^*}{\partial t^{*2}} + \bar{\mu} \frac{\partial X^*}{\partial t^*} + \frac{\partial^4 X^*}{\partial y^{*4}} = \bar{\mu} u^* + \tilde{\rho} \frac{\partial u^*}{\partial t^*}. \tag{14}$$

For small deflections [i.e., using Eq. (6)] the solution is

$$X_{\mathrm{T}}^*(y^*, t^*) = \frac{\int_0^1 F(\xi) Y_1(\xi) d\xi}{\int_0^1 Y_1(\xi)^2 d\xi} \times \frac{Y_1(y^*)}{\sqrt{[({\eta_1}^4 - \hat{\rho})^2 + \bar{\mu}^2]}} \cos(t^* - \alpha)$$
$$- \frac{\tilde{\rho}}{\bar{\mu}} \frac{\int_0^1 F(\xi) Y_1(\xi) d\xi}{\int_0^1 Y_1(\xi)^2 d\xi} \times \frac{Y_1(y^*)}{\sqrt{[({\eta_1}^4 - \hat{\rho})^2 + \bar{\mu}^2]}} \sin(t^* - \alpha), \tag{15a}$$

where $\alpha = \tan^{-1}[\frac{\bar{\mu}}{({\eta_1}^4 - \hat{\rho})}]$. The first term on the right-hand side of Eq. (15a) is the response to the viscous forcing, $\bar{\mu} u^*$, and the second term is the response to the added mass forcing, $\tilde{\rho} \frac{\partial u^*}{\partial t^*}$. The

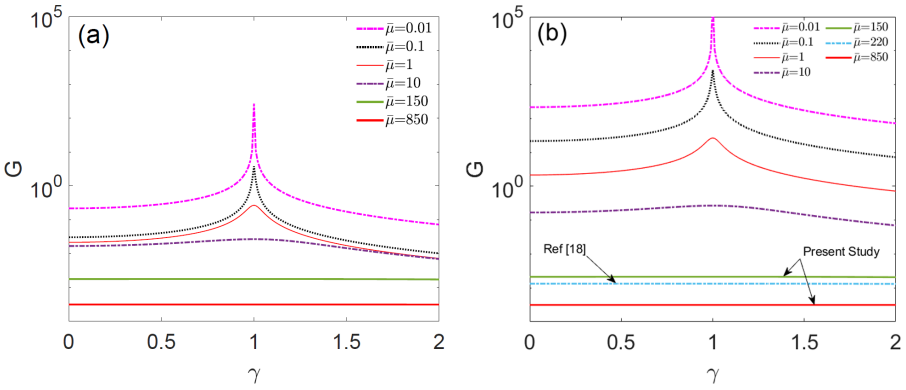

FIG. 4. Transfer function vs frequency ratio at different $\bar{\mu}$. (a) $\tilde{\rho} = 0.1$, (b) $\tilde{\rho} = 100$.

total response is given by the superposition of these two responses. Equation (15a) can be further simplified as

$$X_T^*(y^*, t^*) = \frac{\int_0^1 F(\xi) Y_1(\xi) d\xi}{\int_0^1 Y_1(\xi)^2 d\xi} \times \frac{Y_1(y^*)}{\sqrt{[(\eta_1{}^4 - \hat{\rho})^2 + \bar{\mu}^2]}} \frac{\sqrt{\bar{\mu}^2 + \tilde{\rho}^2}}{\bar{\mu}} \cos(t^* - \alpha + \beta), \tag{15b}$$

where $\beta = \tan^{-1}[\frac{\tilde{\rho}}{\bar{\mu}}]$. This solution precludes the existence of sharp resonance for any finite value of $\bar{\mu}$. In order to elucidate this point further we define a transfer function for the system response using Eq. (13) as follows:

$$G(\bar{\mu}, \gamma) = \frac{\text{Amp}[X_T^*(y^* = 1, t^*)]}{\int_0^1 F(\xi) Y_1(\xi) d\xi} = \frac{1}{\int_0^1 Y_1(\xi)^2 d\xi} \times \frac{Y_1(y^* = 1)}{\sqrt{[(\eta_1{}^4 - \hat{\rho})^2 + \bar{\mu}^2]}} \frac{\sqrt{\bar{\mu}^2 + \tilde{\rho}^2}}{\bar{\mu}}, \tag{16}$$

where Amp[·] denotes the amplitude of [·]. Note that from Eq. (13), we can express $\hat{\rho}$ in terms of ratio of the wave frequency to the natural frequency, $\gamma = \frac{\Omega}{\omega_1}$ as

$$\hat{\rho} = \eta_1{}^4 \gamma^2. \tag{17}$$

Subsequently Eq. (16) can be rewritten as

$$G(\bar{\mu}, \gamma) = \frac{1}{\int_0^1 Y_1(\xi)^2 d\xi} \times \frac{Y_1(y^* = 1)}{\sqrt{\eta_1{}^8 (1 - \gamma^2)^2 + \bar{\mu}^2}} \frac{\sqrt{\bar{\mu}^2 + \tilde{\rho}^2}}{\bar{\mu}}. \tag{18}$$

The transfer function vs the frequency ratio at different values of $\bar{\mu}$ and $\tilde{\rho}$ is shown in Fig. 4. First, it can be observed that increasing the added mass effect leads to an enhanced response of the fiber at a given $\bar{\mu}$. On the other hand, increasing $\bar{\mu}$ at a given $\tilde{\rho}$ leads to a diminished response, as expected. In the present experiments, $\tilde{\rho} \approx 70$–800. For a representative value of $\tilde{\rho} = 100$, as can be seen from Fig. 4(b), for the values of $\bar{\mu}$ corresponding to the present experiments ($\bar{\mu} = 150$–850) the resonance is almost inexistent. It also shows that since the experimental oscillations are in the viscous-dominated regime, there is no possibility of resonance. On the other hand, at very low $\bar{\mu}$, say, at $\bar{\mu} = 0.01$ the resonance is very sharp. From Eq. (12), it can be shown that at $\bar{\mu} = 0$ the transfer function is unbounded at the resonance.

This behavior of the response curve can be further corroborated through the estimation of the quality factor (Q-factor). In order to define the Q-factor we look at the unforced system, namely,

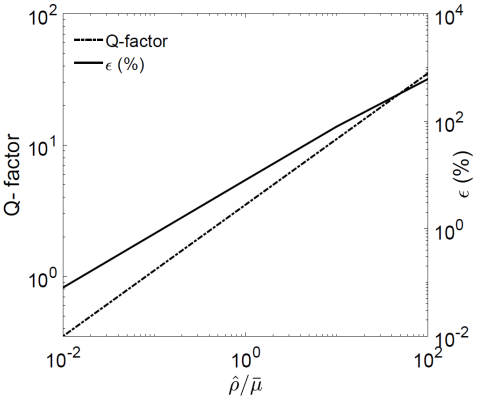

FIG. 5. Q-factor [Eq. (21)] and error vs $\frac{\hat{\rho}}{\bar{\mu}}$.

Eq. (14) with $u^* = 0$ to obtain

$$\hat{\rho}\frac{\partial^2 X^*}{\partial t^{*2}} + \bar{\mu}\frac{\partial X^*}{\partial t^*} + \frac{\partial^4 X^*}{\partial y^{*4}} = 0. \tag{19}$$

Substituting the product solution $Y_1(y^*)T_1(t^*)$, we obtain

$$\hat{\rho}\frac{d^2 T_1}{dt^{*2}} + \bar{\mu}\frac{dT_1}{dt^*} + {\eta_1}^4 T_1 = 0. \tag{20}$$

Subsequently, the Q-factor of the system can be defined by drawing analogy of the above equation with a spring-mass-damper system [23] as follows:

$$Q = \frac{\sqrt{\hat{\rho}{\eta_1}^4}}{\bar{\mu}}. \tag{21}$$

The Q-factor is a measure of the damping of the fiber oscillation and is related to the sharpness of the spectral response of the oscillating fiber. The Q-factor as a function of $\frac{\hat{\rho}}{\bar{\mu}}$ is plotted in Fig. 5. In the inertia-dominated regime (at large values of $\frac{\hat{\rho}}{\bar{\mu}}$), the Q-factor is very large indicating a sharp resonance peak as can be seen in Fig. 4. On the other hand, in the viscous dominated regime (at small values of $\frac{\hat{\rho}}{\bar{\mu}}$), we observe a very low Q-factor and hence no discernible peak in the response curve, as seen in Fig. 4.

Using the in-field experimental conditions used in [18], *viz.*, $C_D = 3$, $\rho_f = 910$ kg/m^3, $r = 0.0025$ m, $f = 1.5$ Hz, $L = 0.8$ m, $u_{\text{tip}} = 0.2$ m/s, $E = 3.9 \times 10^8$ Pa, we get $\bar{\mu} = 220$. This implies that in real-world situations, the oscillations of aquatic plants are in the viscous-dominated regime. $\bar{\mu} = 220$ falls within the range of experimental conditions of the present study, as can be seen in Fig. 4(b). Hence, our results show that the oscillations of sessile aquatic plants in nature, driven by wavy fluid flow, can never exhibit a resonance-like response. We expect their response curve to be similar to the curves corresponding to $\bar{\mu}$ in our experiments in Fig. 4. Moreover, while the viscous forces generate drag on such biological structures, Eq. (15) clearly shows that the same viscous forces cause a reduction in the amplitude of the oscillation of the structures. Note that the structural damping is not considered in our model, which further aids in damping the response and thus decreasing the Q-factor. It is worth mentioning that in real-world situations, the actual excitation could be random, as shown in [18]. However, since the oscillations are linear, the transfer function given by Eq. (18) can be easily extended to predict the response to such a broad-band excitation.

Finally, we estimate the error induced by neglecting inertia and/or added-mass terms in the analysis, which has usually been done in many previous studies (e.g., Refs. [11], [18], and [26]). The

error, which is defined as the relative change in viscous solution [Eq. (11)] from the total solution [Eq. (15b)], is given by

$$\epsilon = \frac{|\mathrm{Amp}[X_V^*(y^*=1,t^*)] - \mathrm{Amp}[X_\mathrm{T}^*(y^*=1,t^*)]|}{\mathrm{Amp}[X_\mathrm{T}^*(y^*=1,t^*)]} \times 100\%. \tag{22}$$

Figure 5 shows the error vs $\frac{\hat{\rho}}{\hat{\mu}}$ and shows that $\frac{\hat{\rho}}{\hat{\mu}} \approx 0.1$ causes an error of 1%. This criterion could serve as a guideline for the future studies to justify the use of a viscous-dominated theory. For instance, for the conditions used in [18], $\frac{\hat{\rho}}{\hat{\mu}} \sim O(0.1)$, which justifies those authors' analysis omitting inertial effects.

V. CONCLUDING REMARKS

In conclusion, the oscillation of a filament induced by a surface gravity wave is studied experimentally and theoretically. We observe that the filament acts as a continuous system undergoing harmonic oscillation driven by the oscillating fluid flow field. An extended Euler-Bernoulli beam model is solved numerically and theoretically. For a wide range of parameters (such as wave frequency, wave number, amplitude, and fluid layer height), the model agrees with experiment both qualitatively and quantitatively, without any fit parameters. The results reveal the absence of resonance in the drag-dominated regime. The response of the fiber with the inclusion of inertia effects is also presented. Based on the in-field experiments carried out in [18], we conclude that oscillation of aquatic plants in real flow scenarios is viscous-dominated and hence cannot exhibit a sharp resonance. The Q-factor of the frequency response of the oscillations further elucidates this point. We also quantified the error incurred in neglecting inertia terms from the analysis. This will help future studies to determine whether the inertia can be neglected. We also observe from the theoretical results that the added mass effect tends to enhance the system response. We hope that our results will contribute to a better understanding of the survival pathways of aquatic plants.

ACKNOWLEDGMENT

Financial support from FIST program of Department of Science and Technology, India is gratefully acknowledged.

[1] F. Lundell, L. D. Söderberg, and P. H. Alfredsson, Fluid mechanics of papermaking, Annu. Rev. Fluid Mech. **43**, 195 (2011).
[2] D. T. Akcabay and Y. L. Young, Hydroelastic response and energy harvesting potential of flexible piezoelectric beams in viscous flow, Phys. Fluids **24**, 054106 (2012).
[3] D. Ambrosi and L. Preziosi, Modeling injection molding processes with deformable porous preforms, SIAM J. Appl. Math. **61**, 22 (2000).
[4] P. Deepu, Cochlear mechanics with fluid viscosity and compressibility, Phys. Rev. E **99**, 032417 (2019).
[5] G. R. Fulford and J. R. Blake, Muco-ciliary transport in the lung, J. Theor. Biol. **121**, 381 (1986).
[6] U. K. Müller, Fish'n flag, Science **302**, 1511 (2003).
[7] M. R. Raupach and A. S. Thom, Turbulence in and above plant canopies, Annu. Rev. Fluid Mech. **13**, 97 (1981).
[8] F. W. Telewski, A unified hypothesis of mechanoperception in plants, Am. J. Bot. **93**, 1466 (2006).
[9] A. Kuparinen, Mechanistic models for wind dispersal, Trends Plant Sci. **11**, 296 (2006).
[10] J. Zhang, S. Childress, A. Libchaber, and M. Shelley, Flexible filaments in a flowing soap film as a model for one-dimensional flags in a two-dimensional wind, Nature (London) **408**, 835 (2000).
[11] M. Shelley, N. Vandenberghe, and J. Zhang, Heavy Flags Undergo Spontaneous Oscillations in Flowing Water, Phys. Rev. Lett. **94**, 094302 (2005).

[12] C. Eloy, R. Lagrange, C. Souilliez, and L. Schouveiler, Aeroelastic instability of cantilevered flexible plates in uniform flow, J. Fluid Mech. **611**, 97 (2008).
[13] S. Jung, K. Mareck, M. Shelley, and J. Zhang, Dynamics of a Deformable Body in a Fast Flowing Soap Film, Phys. Rev. Lett. **97**, 134502 (2006).
[14] S. Vogel, *Life in Moving Fluids: The Physical Biology of Flow* (Princeton University Press, Princeton, 1994).
[15] M. Luhar and H. M. Nepf, Wave-induced dynamics of flexible blades, J. Fluids Struct. **61**, 20 (2016).
[16] T. Leclercq and E. de Langre, Reconfiguration of elastic blades in oscillatory flow, J. Fluid Mech. **838**, 606 (2018).
[17] N. G. Jacobsen, W. Bakker, W. S. J. Uijttewaal, and R. Uittenbogaard, Experimental investigation of the wave-induced motion of and force distribution along a flexible stem, J. Fluid Mech. **880**, 1036 (2019).
[18] J. C. Mullarney and S. M. Henderson, Wave-forced motion of submerged single-stem vegetation, J. Geophys. Res. Oceans **115**, C12061 (2010).
[19] X. Zhang and H Nepf, Flow-induced reconfiguration of aquatic plants, including the impact of leaf sheltering, Limnol. Oceanogr. **65**, 2697 (2020).
[20] P. K. Kundu, I. M. Cohen, and D. R. Dowling, *Fluid Mechanics*, 6th ed. (Academic Press, San Diego, 2012).
[21] P. M. Rao, K. Kuwahara, and K. Tsuboi, Simulation of unsteady viscous flow around a longitudinally oscillating circular cylinder in a uniform flow, Appl. Math. Modell. **16**, 26 (1992).
[22] G. H. Keulegan and L. H. Carpenter, Forces on cylinders and plates in an oscillating fluid, J. Res. Natl. Bur. Stand. **60**, 423 (1958).
[23] L. Meirovitch, *Principles and Techniques of Vibrations* (Prentice-Hall International, Inc., New Jersey, 1997).
[24] F. J. Méndez, I. J. Losada, and M. A. Losada, Hydrodynamics induced by wind waves in a vegetation field, J. Geophys. Res.: Oceans **104**, 18383 (1999).
[25] M. Maza, J. L. Lara, and I. J. Losada, A coupled model of submerged vegetation under oscillatory flow using Navier–Stokes equations, Coastal Eng. **80**, 16 (2013).
[26] S. G. Prasath, J. Marthelot, R. Govindarajan, and N. Menon, Relaxation of a highly deformed elastic filament at a fluid interface, Phys. Rev. Fluids **1**, 033903 (2016).